図13 fMRIを用いて慢性疲労症候群患者の易疲労性に関する研究[18]を行った際にmorphometryの手法で発見した脳萎縮部位

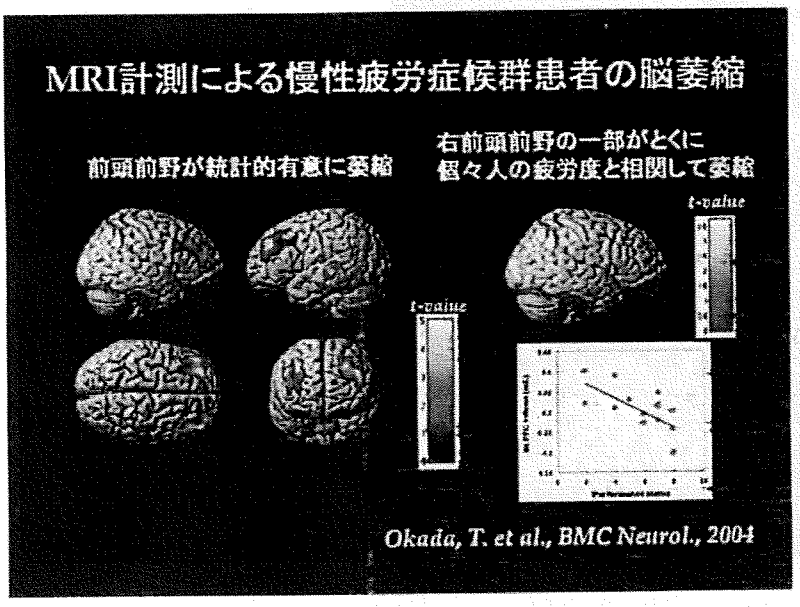


慢性疲労症候群患者には両側の前頭前野に健常者に比し有意な萎縮が見られ，特に右前頭前野の一部では疲労度と相関して萎縮が強い[19]。

図14 これまでの健常者の疲労から慢性疲労症候群患者の脳で見られる知見を整理して作った慢性疲労に陥る神経回路の問題の作業仮説（渡辺による）

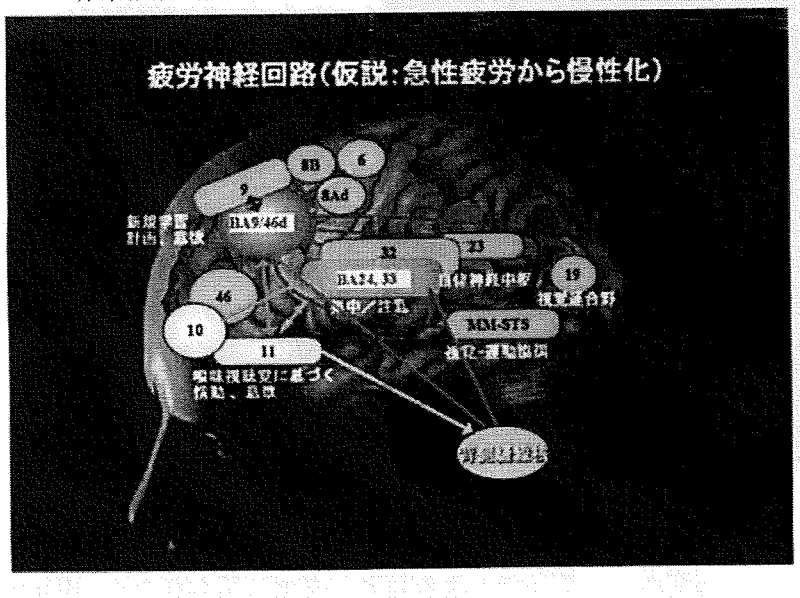


正が起こることが明らかになった．$BH_4$ は，セロトニン系の生合成の補酵素でもあるので，今後は，現在断片的に行われつつあるセロトニン系の発達についても，実際に発達段階に起こっていることを PET 等の非・低侵襲的方法論で追跡していきたい．この例では，治療薬の有効性を実際の患者の脳内の変化で証明できたわけで，治療薬の薬効のメカニズムも実証できることを示している．

## 代謝安定型高速 $^{11}$C−メチル基導入法の開発 ーほとんどすべての有機化合物への [$^{11}$C] 放射性同位元素の導入ー

$^{11}$C の利用は，すべての有機化合物がその構造中に炭素原子を有していることから，低分子化合物の PET プローブ化には理想的なポジトロン崩壊核種である．また，$^{11}$C（半減期約 20 分）を用いると，同じ合成装置で一日に何度も

図15　[$^{11}$C]McN5652 を用いた慢性疲労症候群患者と健常者のセロトニントランスポーターの密度の比較[20]

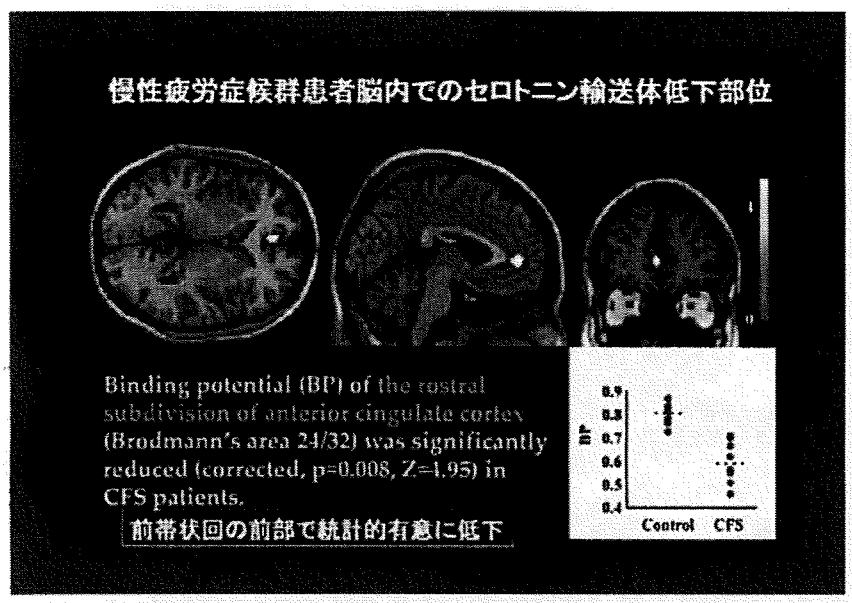


前帯状回の前部でのみ，統計的有意な低下が見られる．

図16 緑の香り（0.03% hexenal と 0.03% hexenol との等量混合物）を与えて，単純作業能率がコントロール匂いより下がらない時のサル PET 脳局所血流量[22]

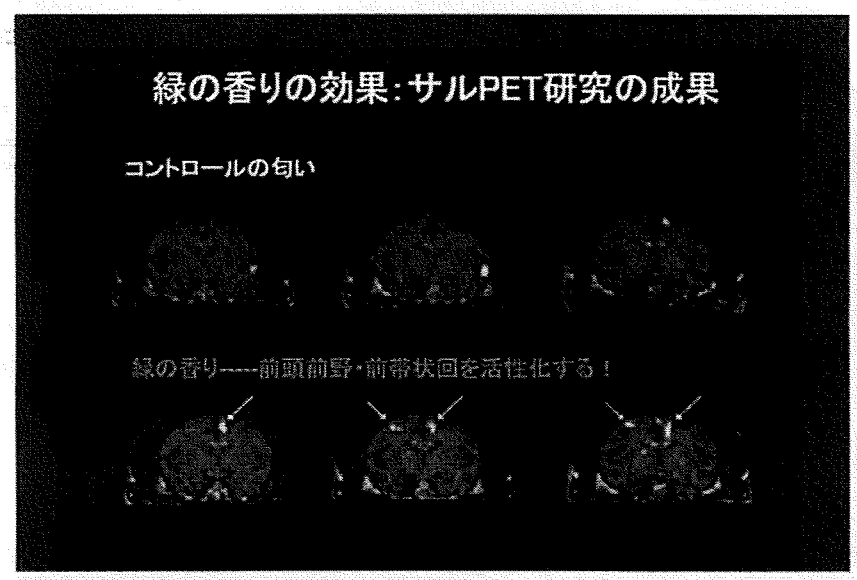


明らかに，ここまで疲労，慢性疲労症候群で問題になってきた前頭前野と前帯状回の活動が緑の香りに支えられていることが興味深い．

サンプル調製が可能であり，放射性副生成物の長期保管の必要もない．このような観点から，我々は短寿命 $^{11}$C の導入をこれまで未知であった炭素－炭素結合形成反応による高速メチル化法により達成しようとした．PET 研究分野では，これまで *O*, *N*, *S* などのヘテロ原子上へのメチル化のみが行われてきたが，上記の高速反応が実現すれば，この新しい $^{11}$C 導入法はこれらの方法を凌駕する多くの利点をもつ．第一に，標識部位は炭素－炭素結合であるため化学的かつ代謝的に安定であり，疾患診断に不可欠な PET 画像の信憑性が保証される．さらに，メチル基は最小の炭素置換基であり，導入位置への自由度が高く，また極性の変化も最小限に留めることができるため，リード化合物の機能（生物活性）の変化を想定の範囲内に設定して PET プローブの設計を行うことができる．すなわち，メチル基が内在する薬剤そのもののみならず新規な創薬候補化合物の迅速なスクリーニングにも最適な方法論となる．

図17 小児自閉症18例のドーパミン系のPET研究

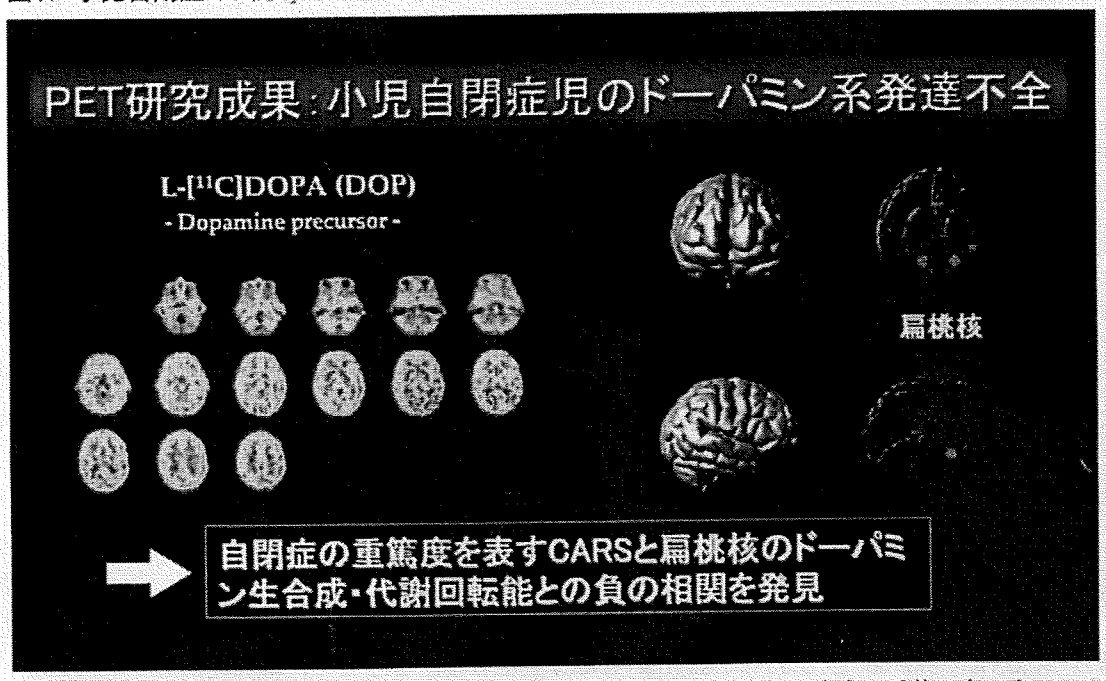


L-[3-$^{11}$C]DOPAの利用能の低下の度合いが大きいほど，自閉症の症状が有意に重篤であった．
(Watanabe, Y. et al., in preparation)

図18 L-[3-$^{11}$C]DOPA-PETで見た小児自閉症患者（3～7歳）に対する6ヶ月間の$BH_4$の治療効果

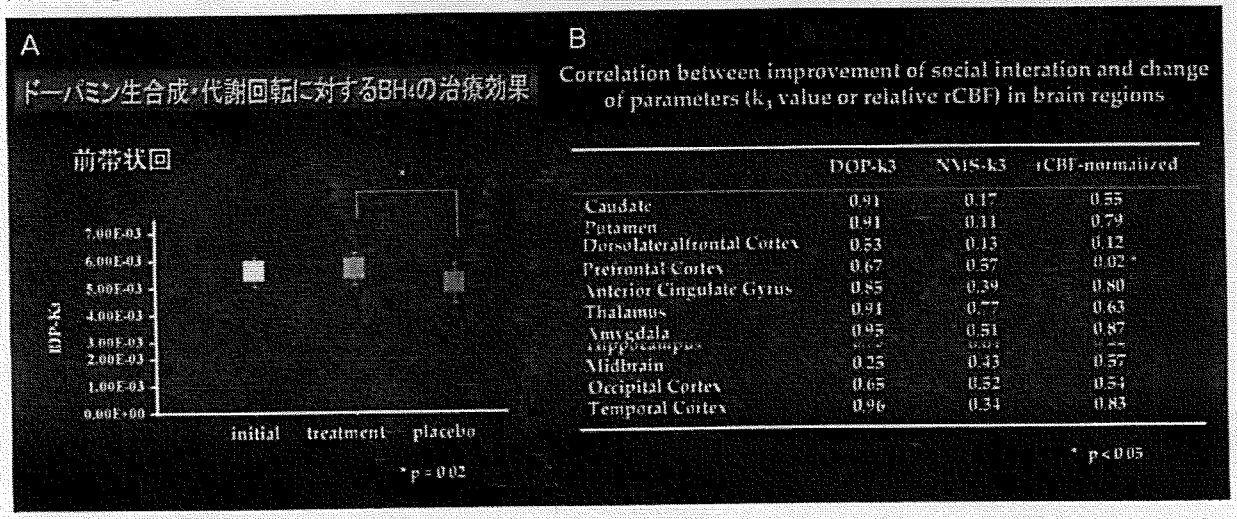


A：ドーパミン生合成能が発達によって減ってくるが，$BH_4$投薬によりそのレベルを保ち続ける作用が判明した．
B：特に，社会性の改善が見られたresponderの脳内では，社会性改善の度合いと前頭前野の血流の改善の度合い，海馬のセロトニン-2受容体の正常化の度合いが有意な相関を示した．

PET研究では放射性合成前駆体（$^{11}CH_3I$など）を大過剰の基質で捕獲するため，その合成条件に合致するように，ヨウ化メチルを過剰量（40当量）の有機スズ化合物で捕捉するStille型高速カップリング反応，すなわち高速メチル化反応の開発を試みた．有機スズ化合物を選択した理由は，① 多くの反応剤や精製資材に対して安定であるため最終段階での放射性同位元素導入反応が可能なこと，② 極めて低極性であり，生成した超微量$^{11}$C標識化合物を大過剰の残存非放射性スズ基質から容易に分離できること，などPETトレーサー合成に合致した最

図19 ほとんどすべての低分子有機化合物への $^{11}C$ 標識法の開発

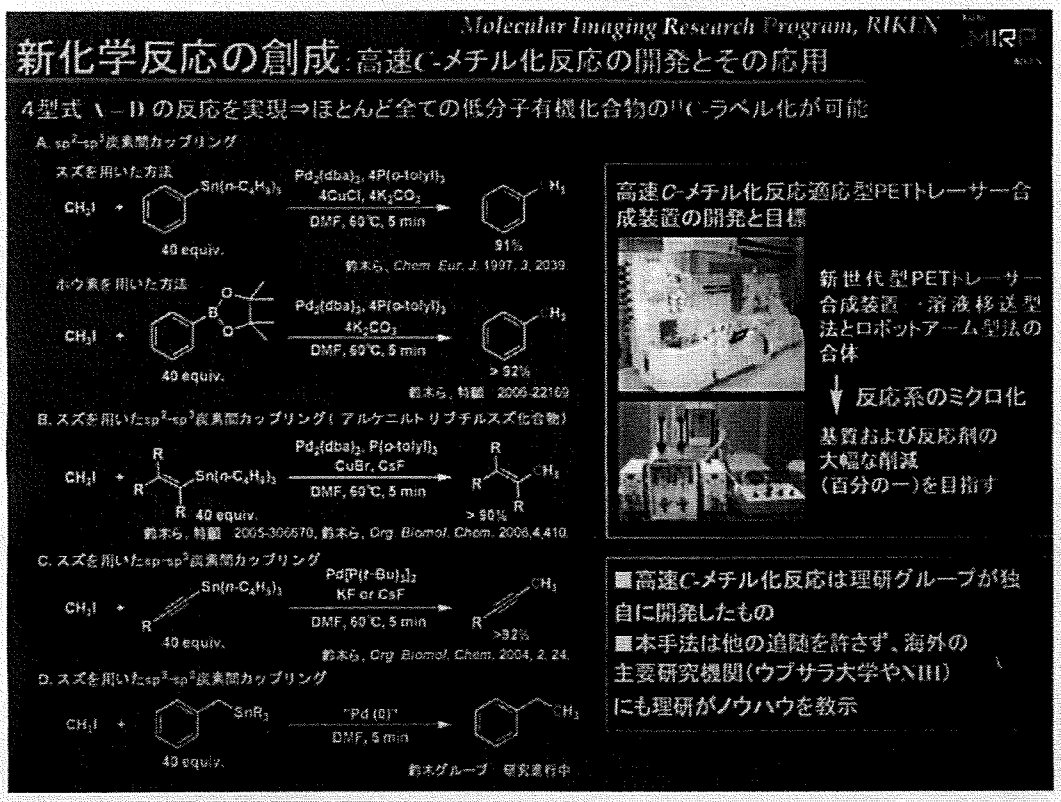


図20 高速 C－メチル化反応により最近開発した $^{11}C$ 標識化合物の例（PET）

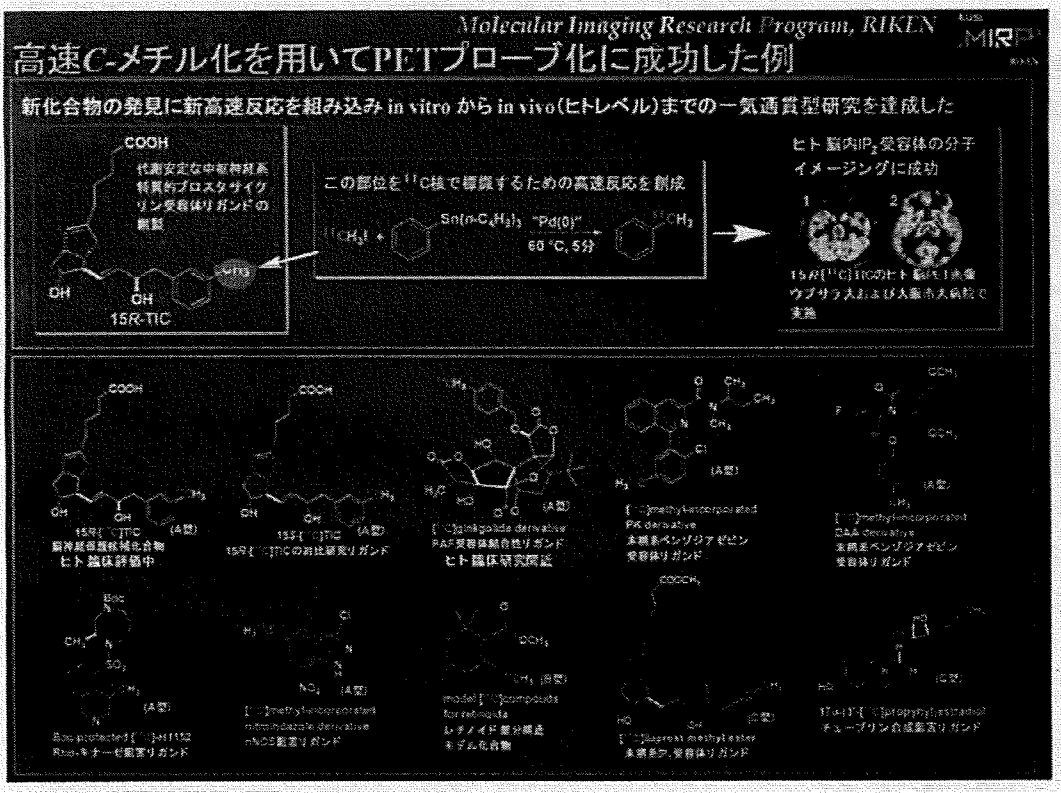

適な捕獲用基質と判断したためである．また，短寿命 PET トレーサーの合成には通常とは異なった化学反応が必要である．半減期がわずか20分である $^{11}C$ の導入の場合には，放射能の急激な減衰のため，反応，精製，そして生体への投与までを半減期の2倍以内に行わなければならない．この全体の制限時間からトレーサーの精製および投与準備時間を差し引くと，$^{11}C$ の導入反応に与えられた時間はわずか5分程度である．

上記のような背景の下，まず非放射化体であるヨウ化メチルを過剰のトリブチルフェニルスズで捕捉する Stille 型 $sp^2$–$sp^3$ カップリングによる高速メチル化反応の開発に挑んだ．数年（～5年）に渡る条件検討の結果，$^{11}C$ を導入した PET 用のトレーサーである 15*R*–[$^{11}C$]TIC メチルエステルの短時間かつ高収率合成を実現した（上述）．さらに，我々は，高速メチル化反応の拡張を行ってきた（図19，論文も図内に記入）．現在，残る $sp^3$–$sp^3$ 高速カップリング研究，および，対象基質の多様性に対応すべくスズ化合物以外の捕捉剤（有機ホウ素化合物など）の使用を検討しているが，いずれも成功裡に進行している．

我々が目的としている図19に示した四型式の高速 [$^{11}C$] メチル化反応が実現すれば，原理的にほとんどすべての有機化合物への $^{11}C$ の導入（PET トレーサー化）が可能であり，PET 研究によりヒトまで含めた対象薬剤の体内動態がわかる．このような新しい化学反応を開発して，様々な化合物を動物・ヒトの PET に続々と導入中（図20）で，今後，500種程度の創薬候補化合物が $^{11}C$ の導入を待っている状況である．また *C*–メチル化反応は，$^{13}CH_3$，$^{14}CH_3$，および $CD_3$ 基の導入にももちろん適用可能であり，今後，様々な角度からの薬物代謝研究に役立つ．特に $^{14}CH_3$ 基の導入は，Accelerator Mass Spectrometry（AMS 法，$10^{-18}$～$10^{-21}$ M の $^{14}C$–enrich した超微量の薬物サンプルを使用した質量分析法で，被曝量が少なくヒトにも適用可能）による長期間の薬物代謝解析研究に有効である．

## タンパク質・ペプチド・糖鎖・核酸塩基配列（DNA/RNA）を標識した分子イメージング研究

分子イメージングの方法論をさらに汎用化・網羅化するためには，高分子物質にも標識が行われ，本来の機能・生理活性・結合能などを損なわない方法論の開発が重要である．この点でも現在，我々は様々な方法論とそのための自動合成装置（実験者の被曝を最小限にする）の開発研究（図21）を行っている．

タンパク質では，主には，幹細胞認識のための抗 CD133 抗体，細胞障害性ヘルパーT細胞の認識に抗 CD34 抗体，扁平上皮癌に対する抗 EGF–R 抗体などを標識して，細胞種別 PET 研究を行っている．ペプチドに関しては，サイトカイン・ケモカイン，神経内分泌ペプチドをはじめ多くの活性ペプチドが標的であり，ソマトスタチンやその代謝耐性型のオクトレオタイドなどの $^{68}Ga$ 標識を進めた．さらに核酸配列や糖鎖への標識には，核酸化学，糖鎖工学，ケミカルバイオロジーの最先端化学者と共同して新規標識法を開拓し，PET 研究を進めている．

## 薬物動態予測のための薬物トランスポータープローブの開発とリソース化

東京大学大学院薬学系研究科，放医研，理研の共同研究として，薬物の動態予測に資する10数種の（すでに分子構造が解明され比較的特異的なリガンドを有する）薬物トランスポーターに対する分子イメージングプローブの開発を放医研および理研で分担して開始した．放医研では，まず BCRP トランスポーター解析用候補化合物として $^{13}N$–標識ダントロレンの合成を行い，正常マウスを用いた PET 計測を行った．現在，基礎的評価を始めている．理研側では，高速 *C*–*C*–メチル化反応を用いて，OATP1B1，OAT3，MRP2 トランスポーター解析用候補化合物としてプラバスタチンの標識合成に着手した．本研究のユニークな点は，安全性が保証さ

れ薬理量が実際にヒトで利用されている既存の薬物を標識して行う研究であるので，動物実験直後に直截にヒトの分子イメージング研究に展開できることである．今後，順次異なった薬物トランスポーターに対する候補化合物の標識合成を行い，個々の薬物トランスポーターノックアウトマウス等を用いて PET により解析し，医薬品開発に資するトランスポーター解析ツールを3者の共同研究により確立する．

## 小動物 PET 計測の最適化

創薬や分子イメージング技術開発に，小動物用の microPET 研究は必須である．我々は，2000年に大阪市立大学に世界第1号機となった microPET を導入したので，和田を中心として，実際の動物実験における microPET 計測に関する諸条件の最適化を図り，画像データ解析法の向上を図ってきた[25]．超高分解能画像の定量性確保，収集データの高品質化（散乱，ランダムの減少）を行うための具体的な策を見つけ，また，画像間演算による新しい生物学的パラメーターの抽出法を創案する研究である．これまでに，microPET 計測にかかる減弱補正の検討や鉛シールドの適用を行い，定量的・高精度の画像を得ることに成功した．最近では，さらに，理研神戸研の分子イメージング研究プログラム新施設に新規に導入された microPET Focus220 の基本的検討（図22）を行うとともに，PET トレーサーの薬物動態の可視化に成功した．従来定量性が低いと言われている統計学に基づく画像再構成法のパラメーター・スキャン条件・画像分解能・統計ノイズとの関連性を調べ，高定量である条件を見つけることに成功し，実際のイメージングでの研究を開始した（図23）．3次元的に分布している薬物の動態データを Maximum Intensity Projection（MIP）画像を用いて分かりやすく表示する方法を開発し，遺伝子発現・分子認識・細胞分別・代謝変換分子および薬物到達・薬物動態解析イメージングで実際に使用を開始している．

## コンプトンカメラを利用した複数分子同時イメージング法の開発

同一個体を用いた時差複数分子イメージングを行ってきて，その実例もいくつか挙げてきたが，実際に分子イメージングを行っていくと，病態把握や治療効果モニターなどにおいては，複数分子を同時にイメージングできることの重要さに気づく．GREI（Ge 半導体コンプトンカメラによるγ線エミッションイメージング装置）開発による同時複数分子イメージングなど，PET 用分子プローブの適用も視野に入れて，新規のイメージング法の開発にも取り組んできた．和光研究所仁科加速器研究センター RI 製造応用チーム 榎本副チームリーダー，本村基礎科学特別研究員らとの共同研究の中で，技術的開発として，装置の改良，高度化に資するため XY ステージを導入し，スキャン撮像の実現に成功した．また，3次元画像再構成アルゴリズムの改良と高速化を行い，DOI 測定によるγ線相互作用位置の深さ方向の測定精度1 mm 以下を達成した．さらに，低エネルギーγ線撮像のための Si 検出器の導入と，現 Ge コンプトンカメラとの融合に関する特許を出願（2006-220446）した．

一方，GREI による基礎医学的研究においては，GREI 画像と PET 画像の融合を目指しており，現在までに，既存核医学製剤を用いた小動物における複数分子同時イメージングに成功している．すなわち，麻酔下の正常 ICR マウス（8週齢・♂）に，$^{65}ZnCl_2$，$^{85}SrCl_2$，$^{131}I$-ヨウ化メチルノルコレステロールを投与し，GREI による同時撮像を行った．それぞれの製剤の投与量・投与時間は，2 MBq/撮像 30 分前，2 MBq/撮像1日前および 18.7MBq/撮像 5，4，3 日前である．副腎シンチグラフィーに臨床応用されている $^{131}I$-ヨウ化メチルノルコレステロールは3日に分けて分割投与した．マウスはネンブタール麻酔状態で 12 時間連続撮像し，その後，連続蓄積撮像のため屠殺して，24 時間の蓄積像を撮像した．この後，解剖して各臓器中

図21 生体高分子標識のための $^{68}$Ga 標識法の開発と自動合成装置

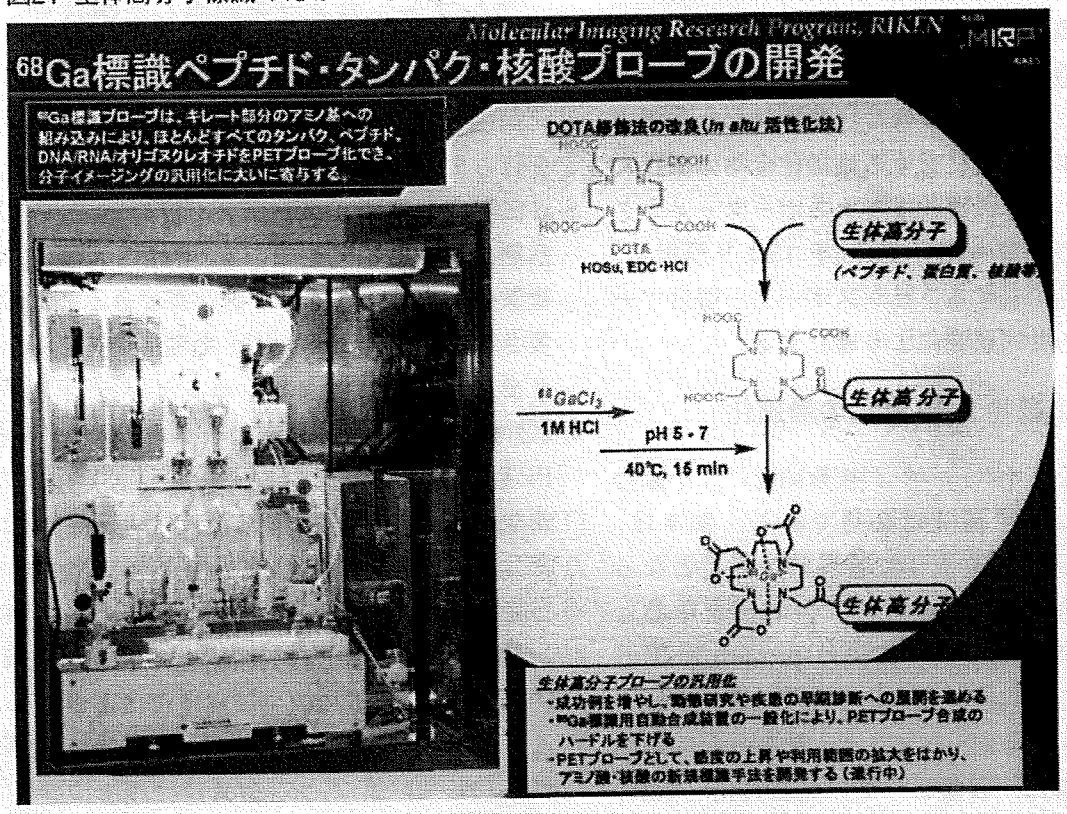


図22 microPET P4 と microPET focus220 による計測を最適化

| | microPET P4 | microPET Focus220 |
|---|---|---|
| Crystal Material | LSO | LSO |
| Detector Diameter (cm) | 26 | 26 |
| Axial Field of View (cm) | 7.8 | 7.6 |
| Total Number of LSO Elements | 10,752 | 24,192 |
| Crystal Size (mm) | 2.2 x 2.2 x 10.0 | 1.5 x 1.5 x 10.0 |
| Packing Fraction (%) | 80 | 92 |
| Number of Slices | 63 | 95 |
| Slice Pitch (mm) | 1.215 | 0.815 |

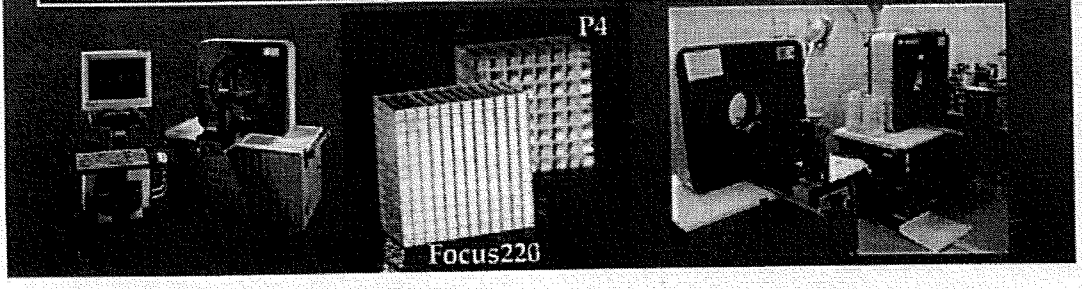

図23 ラット脳 FDG−microPET 画像の最適化例

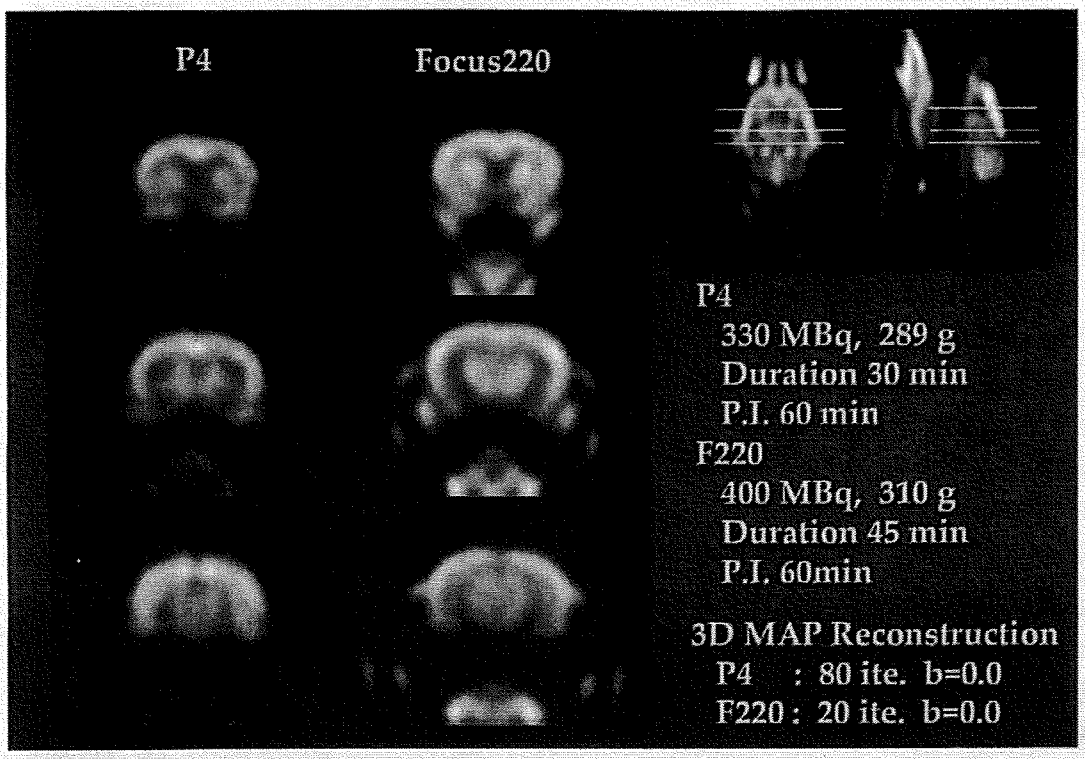


図24 世界初の複数分子同時イメージング成功画像

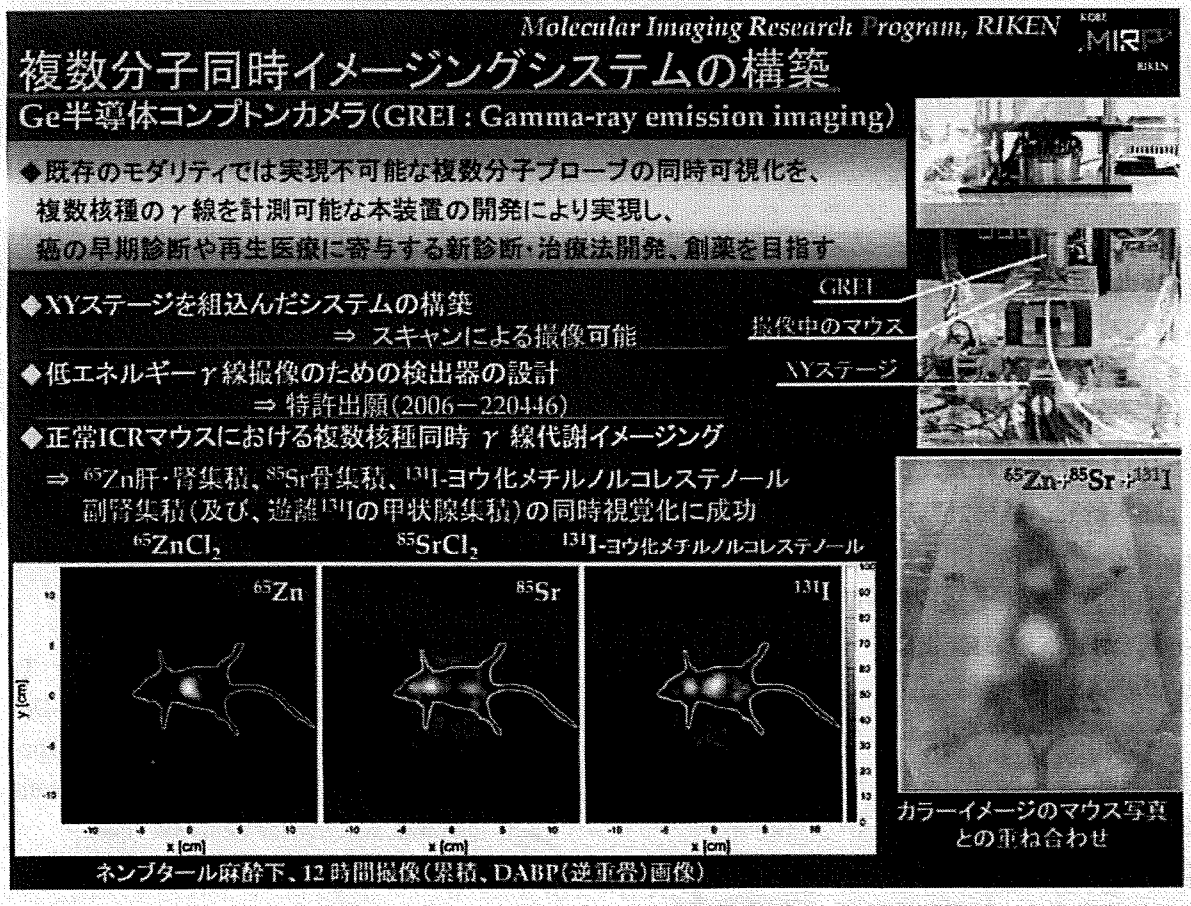

の放射能を Ge 半導体検出器で測定し，核種分布を測定した．図24に $^{65}$Zn（γ線エネルギー：1,115keV），$^{85}$Sr（514keV），$^{131}$I（364.5keV）3核種の同時イメージング像を示す．図から明らかなように，$^{65}$Znの肝・腎集積，$^{85}$Srの骨集積，$^{131}$I-ヨウ化メチルノルコレステロールの副腎への高集積および遊離 $^{131}$Iの甲状腺集積を同時に可視化することに成功した．この結果は，個別臓器の核種分布測定結果と一致し，時間依存的な代謝イメージングの結果と一致した．今後はこの結果を踏まえて，PET 用分子プローブと既存核医学製剤，マルチトレーサーなどの複数分子プローブを用いた複数核種の同時イメージング実験を推進し，病態モデル動物を用いて臨床応用を見据えた複数分子プローブの提案を試みる．また，装置開発と実用化の検討においては，TOI を実装し，既存モダリティと現装置の比較，低エネルギーγ線対応型 Si/Ge の開発のためのシミュレーションを行い，臨床用装置開発を行っていく．また，宇宙開発機構（JAXA）の開発した Si/CdTe 検出器による小動物複数分子同時イメージングに着手し，簡易型コンプトンカメラの開発と改良を実施する．

## 結 び

以上のように，分子イメージング研究が創薬や疾患診断に有用であるということについては言を待たない．それらの実例を積み上げていく努力が必要とされる．しかし，機器開発，計測法，数量モデルデータ解析法，化学，分子設計，分子プローブ機能評価，疾患モデル動物での研究，臨床研究，多施設臨床研究標準化，新しい regulation 作成，等々，この分野にはまだまだ多数の研究と人材が必要であり，それらを融合・統合するための確実なロードマップと研究プログラムが必須である．

謝 辞

これまで研究の機会を与えていただき，また，温かくご指導・ご支援いただきました早石 修先生，井村裕夫先生，野依良治先生，玉尾皓平先生，野口照久先生，花房秀三郎先生に，心より感謝致します．文部科学省分子イメージング研究プログラム担当官の方々，横山哲夫 PD，杉山雄一 PO，井戸達雄 PO，科学技術振興機構の担当官の方々，理化学研究所理事の諸先生をはじめ，プライオリティ会議，経営企画部，知的財産戦略センター，神戸研究所，分子イメージング研究プログラム，仁科加速器研究センターの先生方，スタッフの方々に感謝致します．また，大阪市立大学大学院医学研究科，岐阜大学鈴木研究室の先生方，スタッフの方々，先端医療センターはじめ共同研究者の皆様に感謝致します．

## 文 献

1) Matsumura K, Watanabe Yu, Onoe H, Watanabe Y: Prostacyclin receptor in the brain and central terminals of the primary sensory neurons: an autoradiographic study using a stable analogue [$^3$H]iloprost. Neuroscience 65: 493–503, 1995.
2) Takechi H, Matsumura K, Watanabe Yu, Kato K, Noyori R, Suzuki M, Watanabe Y: A novel subtype of the prostacyclin receptor expressed in the central nervous system. J Biol Chem 271: 5901–5906, 1996.
3) Watanabe Yu, Matsumura K, Takechi H, Kato K, Morii H, Björkman M, Långström B, Noyori R, Suzuki M, Watanabe Y: A novel subtype of prostacyclin receptor in the central nervous system. J Neurochem 72: 2583–2592, 1999.
4) Suzuki M, Kato K, Noyori R, Watanabe Yu, Takechi H, Matsumura K, Långström B, Watanabe Y: (15R)-(*m*-Tolyl)-17, 18, 19, 20-tetranorisocarbacyclin. A stable ligand with high binding affinity and specificity for a prostacyclin receptor in the central nervous system. Angewandte Chemie 35: 334–336, 1996.
5) Suzuki M, Kato K, Watanabe Yu, Satoh T, Matsumura K, Watanabe Y, Noyori R: 15-Deoxy-16-(m-tolyl)-17, 18, 19, 20-tetranorisocarbacyclin: a simple TIC derivative with potent anti-apoptotic activity for neuronal cells. Chem Commun: 307–308, 1999.

6) Satoh T, Ishikawa Y, Kataoka Y, Cui Y, Yanase H, Kato K, Watanabe Yu, Nakadate K, Matsumura K, Hatanaka H, Kataoka K, Noyori R, Suzuki M, Watanabe Y: CNS-specific prostacyclin ligands as a novel class of candidates for therapeutic agents against neuronal death. Eur J Neurosci 11: 3115-3124, 1999.

7) Cui Y, Kataoka Y, Satoh T, Yamagata A, Shirakawa N, Watanabe Yu, Suzuki M, Yanase H, Kataoka K, Watanabe Y: Protective effect of prostaglandin $I_2$ analogs on ischemic delayed neuronal damage in gerbils. Biochem Biophys Res Commun 265: 301-304, 1999.

8) Takamatsu H, Tsukada H, Watanabe Yu, Cui Y-L, Kataoka Y, Hosoya T, Suzuki M, Watanabe Y: Specific ligand for a central type prostacyclin receptor attenuates neuronal damage in a rat model of focal cerebral ischemia. Brain Res 925: 176-182, 2002.

9) Frykholm P, Andersson J L R, Valtysson J, Silander H C, Hillered L, Persson L, Olsson Y, Yu W R, Westerberg G, Watanabe Y, Långström B, Enblad P: A metabolic threshold for irreversible ischemia demonstrated by PET in a middle cerebral artery occlusion-reperfusion primate model. Acta Neurol Scand 102: 18-26, 2000.

10) Enblad P, Frykholm P, Valtysson J, Silander H C, Andersson J, Fasth K J, Watanabe Y, Långström B, Hillered L, Persson L: Middle cerebral artery occlusion and reperfusion in primates monitored by microdialysis and sequential positron emission tomography. Stroke 32: 1574-1580, 2001.

11) Cui Y L, Takamatsu H, Kakiuchi T, Ohba H, Kataoka Y, Yokoyama C, Onoe H, Watanabe Yu, Hosoya T, Suzuki M, Noyori R, Tsukada H, Watanabe Y: Neuroprotection by a central nervous system-type prostacyclin receptor ligand demonstrated in monkeys subjected to middle cerebral artery occlusion and reperfusion: A positron emission tomography study. Stroke 37: 2830-2836, 2006.

12) Suzuki M, Doi H, Kato K, Björkman M, Långström B, Watanabe Y, Noyori R: Rapid methylation for the synthesis of a $^{11}C$-labeled tolylisocarbacyclin imaging the $IP_2$ receptor in a living human brain. Tetrahedron 56: 8263-8273, 2000.

13) Watanabe Y, Långström B, Stålnacke C-G, Gullberg P, Svärd H, Halldin C, Hayaishi O: Synthesis of $^{11}C$-labeled prostaglandins and positron emission tomography studies using the rhesus monkey. Adv Prostaglandin Thromboxane Leukot Res 17B: 943-945, 1987.

14) Klunk W E, Engler H, Nordberg A, et al: Imaging brain amyloid in Alzheimer's disease with Pittsburgh Compound-B. Ann Neurol 55: 306-319, 2004.

15) Shimada H, Ataka S, Yoshioka E, Ishii H, Kawabe J, Wada Y, Takeda K, Tamura A, Masaki H, Tsutada T, Shimonishi S, Shiomi S, Miki T, Mori H, Watanabe Y: (manuscript in preparation). 日本神経学会 2007 特別講演, 2007 年 5 月 17 日 名古屋国際会議場.

16) Tanaka M, Nakamura F, Mizokawa S, Matsumura A, Nozaki S, Watanabe Y: Establishment and assessment of a rat model of fatigue. Neurosci Lett 352: 159-162, 2003.

17) Kuratsune H, Yamaguti K, Lindh G, Evengård B, Hagberg G, Matsumura K, Iwase M, Onoe H, Takahashi M, Machii T, Kanakura Y, Kitani T, Långström B, Watanabe Y: Brain regions involved in fatigue sensation: Reduced acetylcarnitine uptake into the brain. Neuroimage 17: 1256-1265, 2002.

18) Tanaka M, Sadato N, Okada T, Mizuno K, Sasabe T, Tanabe H C, Saito D N, Onoe H, Kuratsune H, Watanabe Y: Reduced responsiveness is an essential feature of chronic fatigue syndrome: A fMRI study. BMC Neurol 6: 9, 2006.

19) Okada T, Tanaka M, Kuratsune H, Watanabe Y, Sadato N: Mechanisms underlying fatigue: a voxel-based morphometric study of chronic fatigue syndrome. BMC Neurol 4: 14, 2004.

20) Yamamoto S, Ouchi Y, Onoe H, Yoshikawa E, Tsukada H, Takahashi H, Iwase M, Yamaguti K, Kuratsune H, Watanabe Y: Reduction of serotonin transporters of patients with chronic fatigue syndrome. Neuroreport 15: 2571-2574,

2004.
21) Narita M, Nishigami N, Narita N, Yamaguti K, Okado N, Watanabe Y, Kuratsune H: Association between serotonin transporter gene polymorphism and chronic fatigue syndrome. Biochem Biophys Res Commun 311: 264–266, 2003.
22) Sasabe T, Kobayashi M, Kondo Y, Onoe H, Matsubara S, Yamamoto S, Tsukada H, Onoe K, Watabe H, Iida H, Kogo M, Sano K, Hatanaka A, Sawada T, Watanabe Y: Activation of the anterior cingulate gyrus by 'Green Odor': A positron emission tomography study in the monkey. Chem Senses 28: 565–572, 2003.
23) Fernell E, Watanabe Y, Adolfsson I, Tani Y, Bergström M, Lilja A, Hartvig P, von Knorring A–L, Gillberg C, Långström B: Possible effects of tetrahydrobiopterin treatment in six children with autism – clinical and positron emission tomography data: a pilot study. Dev Med Child Neurol 39: 313–318, 1997.
24) Danfors T, von Knorring A–L, Hartvig P, Langstrom B, Moulder R, Stromberg B, Torstenson R, Wester U, Watanabe Y, Eeg–Olofsson O: Tetrahydrobiopterin in the treatment of children with autistic disorder: a double–blind placebo–controlled crossover study. J Clin Psychopharmacol 25: 485–489, 2005.
25) Matsumura A, Mizokawa S, Tanaka M, Wada Y, Nozaki S, Nakamura F, Shiomi S, Ochi H, Watanabe Y: Assessment of microPET performance in analyzing the rat brain under different types of anesthesia: Comparison between quantitative data obtained with microPET and *ex vivo* autoradiography. Neuroimage 20: 2040–2050, 2003.

---

## Innovative Molecular Imaging Research for Efficient Drug Development and Diagnosis

Yasuyoshi Watanabe[1,2], Masaaki Suzuki[1,3], Hirotaka Onoe[1], Hisashi Doi[1], Yasuhiro Wada[1], Yosky Kataoka[1,2], Shuichi Enomoto[1,4]

[1] Molecular Imaging Research Program, RIKEN
[2] Osaka City University Graduate School of Medicine
[3] Gifu University Graduate School of Medicine
[4] Metallomics Research Unit, RIKEN Wako Institute

# Gamma-Ray Compton Imaging of Multitracer in Biological Samples Using Strip Germanium Telescope

Shinji Motomura, Shuichi Enomoto, Hiromitsu Haba, Kaori Igarashi, Yasuyuki Gono, and Yasushige Yano

*Abstract*—**The feasibility of using a Compton camera for multitracer imaging has been demonstrated with the results of two biological sample imaging experiments. The distribution of the multitracer administered to a soybean sample and a tumor-bearing mouse has been visualized for each nuclide simultaneously. Three-dimensional images of the multitracer have been obtained even though the samples were measured from a fixed direction.**

*Index Terms*—**Biomedical nuclear imaging, Compton camera, germanium radiation detectors, multitracer.**

## I. Introduction

THE multitracer, which was invented at RIKEN in 1991 [1], is a powerful tool for investigating the behavior of various chemical elements in a sample. It is produced by irradiating a metal target with a heavy-ion beam accelerated to an energy of 135 MeV/u, and then chemically processing the various radioactive nuclides produced mainly through the nuclear-fragmentation reaction, into the final form of a multitracer solution. Since the multitracer contains the radioisotopes of various elements, the information regarding the radioisotopes under the same conditions can be obtained simultaneously by a single experiment. Moreover, the multitracer enables us to observe the correlated behavior among many elements. This information can never be obtained by combining the data of many single-tracer experiments. Owing to these advantages, the multitracer has found many applications in biology, medicine, environmental science, and other fields [2].

Although the potential advantages of multitracers are promising, no nondestructive inspection method has yet been established to realize their full potential particularly for in vivo imaging. This is because the multiple $\gamma$ rays emitted from the multitracer span an energy range from ~100 keV to 2 MeV. For energies above ~300 keV, sufficient spatial resolution cannot be obtained by a conventional $\gamma$-ray imager equipped with mechanical collimators. In addition, the energy resolution must be high enough to distinguish each nuclide contained in the multitracer.

In this paper, we describe a prototype of a Compton camera for mutlitracer imaging, which we call GREI (Gamma-Ray Emission Imaging), and present some results of test experiments with biological samples. The original idea of the Compton camera was invented in the early 1970s [3], and it was soon proposed for medical imaging [4]. Since then, various types of Compton cameras have been proposed for various uses [5].

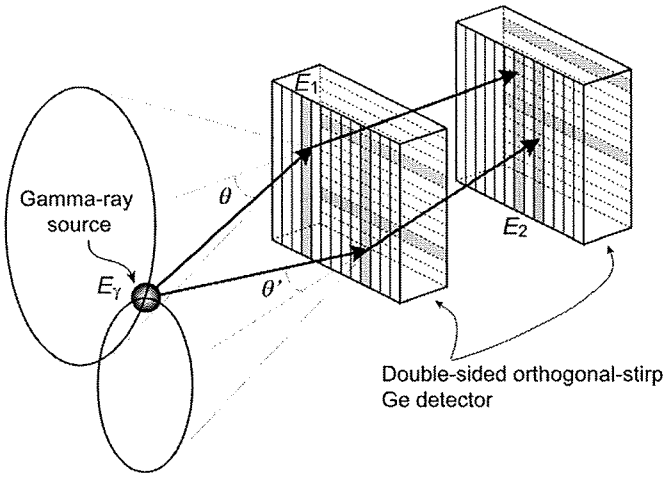


Fig. 1. Schematic of the strip Ge telescope operated as a Compton camera.

Previously, we performed a test experiment using a Compton camera composed of two segmented germanium (Ge) detectors [6]. Owing to the excellent energy resolution of the Ge detectors, three $\gamma$-ray sources of $^{60}$Co, $^{137}$Cs and $^{152}$Eu were clearly distinguished by setting energy windows on the corresponding $\gamma$-ray photopeaks, and their positions were simultaneously determined. The GREI system described in this paper has been modified taking into account the results of the test experiment, further simulations [7], and recent technologies developed for $\gamma$-ray detection [8]–[12].

## II. Description of the GREI System

The GREI system is composed of two double-sided orthogonal-strip Ge detectors manufactured by Eurisys Mesures (Fig. 1). The detectors are arranged parallel to each other and mounted in a single cryostat. The dimensions of the active volume of the Ge crystals are 39 mm × 39 mm × 10 mm and 39 mm × 39 mm × 20 mm for the front and rear detectors, respectively. The strip pitch is 3 mm for both detectors. The center-to-center distance between the crystals is 60 mm.

The electronics are schematically shown in Fig. 2. Conventional circuit modules based on NIM and CAMAC standards

Manuscript received November 14, 2004; revised January 24, 2007. This work was supported in part by the Special Postdoctoral Researchers Program of RIKEN.

The authors are with the Cyclotron Center, RIKEN, Wako, Saitama 351-0198, Japan (e-mail: motomura@riken.jp).

Digital Object Identifier 10.1109/TNS.2007.894209

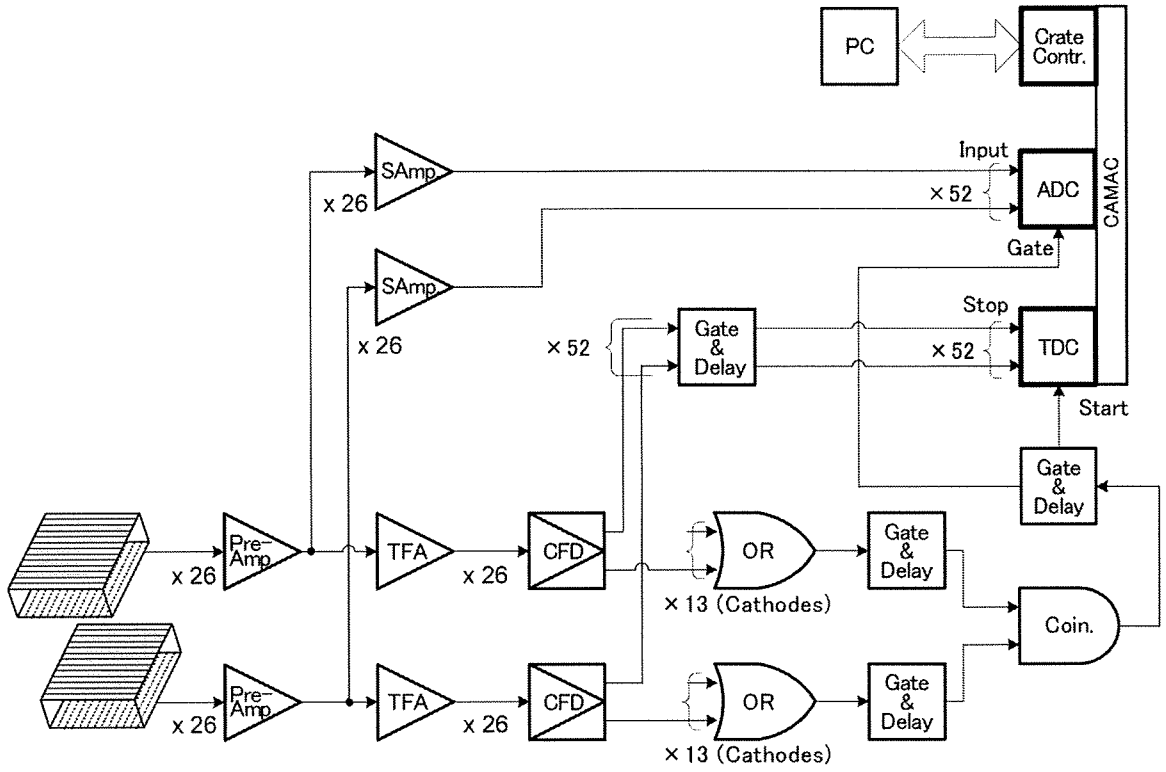


Fig. 2. Circuit diagram of the current prototype of the GREI system. The circuit modules are based on NIM and CAMAC standards.

are used. All the output signals of the preamplifiers are fed into the constant fraction discriminators (CFDs) through the timing filter amplifiers (TFAs), and the timing pulses are generated. All the timing pulses are fed into the time-to-digital converters (TDCs) to digitize the timing signals. To select the Compton scattering events, the timing pulses derived from the cathode strips are used to perform coincidence measurement between the front and rear detectors.

All the output signals of the preamplifiers are also fed into the shaping amplifiers to generate slow signals for energy measurement. Then the pulse heights are digitized by the analog-to-digital converters (ADCs).

In the current implementation, the transverse position of the $\gamma$-ray interaction is determined by a combination of the anode and cathode strips with the accuracy given by the width of the strip. On the other hand, the depth position of the $\gamma$-ray interaction in the Ge crystal can be determined more accurately than the thickness of the crystal, by taking into account the time difference between the signals from the anode and cathode strips [8]–[12]. To realize accurate depth measurement, the time constants of TFAs were set to 500 ns and 60 ns for differentiation and integration, respectively. Delay time of the CFDs was set to 50 ns, which was the upper limit of the modules, and the fraction of the CFDs was set to 0.5.

The digitized data of the TDCs and ADCs are transferred event by event to the personal computer. The transferred data are analyzed on-line, and also recorded in list mode for further off-line analysis. If an incident $\gamma$ ray is Compton scattered in the front detector and deposits energy $E_1$, and then the scattered $\gamma$ ray is fully absorbed in the rear detector and deposits energy $E_2$, the original $\gamma$-ray energy $E_\gamma$ is obtained by summing $E_1$ and $E_2$. Thus, the nuclides contained in the multitracer are distinguished by setting energy windows at the corresponding energy peaks in the $E_\gamma$ spectrum. Throughout this paper, the range of an energy window was $\pm$ 5 keV of the peak position and the windows were applied in the software.

## III. Implementation of Image Reconstruction Methods

For image reconstruction, we are currently employing a two-step method. In the first step, an intermediate image, which is called a simple back-projection (SBP) image, is constructed by simply accumulating the back-projections over all detected events, using an algorithm analogous to the cone-surface mapping algorithm [13]. The back-projection for one event is a cone surface that indicates the possible position of the $\gamma$-ray source. The cone axis is the straight line passing through the first and second interaction points. The half-cone angle $\theta$ is the Compton scattering angle determined by the following equation:

$$\cos\theta = 1 + m_e c^2 \left( \frac{1}{E_\gamma} - \frac{1}{E_\gamma - E_1} \right), \tag{1}$$

where $m_e c^2$ is the rest-mass energy of an electron.

Here, we adopt a model that the SBP image is constructed by linear mapping of the source distribution image; that is,

$$n_i = \sum_j p_{ij} \lambda_j, \tag{2}$$

where $n_i$ is the value of voxel $i$ in the SBP image, $\lambda_j$ is the value of voxel $j$ in the source distribution image, $p_{ij}$ is the point-spread function (PSF), or the point kernel function [13], which represents the SBP image of the point source at voxel $j$; the three-dimensional (3D) coordinates are represented by the single indices $i$ and $j$. In general, the shape of the PSF varies depending on the source position, because the range of the accepted incident angle and scattering angle of $\gamma$ rays depends on the source position. Therefore, a spatially variant PSF must be used to perform rigorous image reconstruction. However, the PSF should be approximated by a spatially invariant PSF within a local region.

Then the second step is to deconvolve the SBP image with the PSF. We have implemented an analytical algorithm and an iterative algorithm for the deconvolution.

If the PSF is assumed to be spatially invariant, $\lambda_j$ can be reconstructed analytically by adopting the Fourier convolution theorem. The matrix $p_{ij}$ is diagonalized by taking the Fourier transform of both sides of (2), and then $\lambda_j$ is obtained in the spatial frequency domain as follows:

$$\lambda_j = \frac{n_j}{p_{jj}}. \tag{3}$$

In most cases, an additional filter function $(w_j)$ must be multiplied to the right side of (3) in order to suppress the statistical noise components, which are dominant in the high-frequency regions, that is:

$$\lambda_j = \frac{w_j n_j}{p_{jj}}. \tag{4}$$

If a Wiener filter function can be designed for the system, (4) becomes the optimal estimation in terms of the least square errors. In addition, ad hoc filter functions, such as a Butterworth function, can be used for $w_j$ to suppress the noise components in the high-frequency regions.

We have also implemented an iterative deconvolution algorithm, which was adapted from the additive SIRT algorithm [14]. First, an initial estimate of the original image $\lambda_j^{(0)}$ is obtained by averaging the SBP image:

$$\lambda_j^{(0)} = \frac{1}{N}\sum_{i=1}^{N} n_i. \tag{5}$$

Then the (n+1)-th estimate $(\lambda_j^{(n+1)})$ is obtained from the n-th estimate $(\lambda_j^{(n)})$ as follows:

$$\lambda_j^{(n+1)} = \lambda_j^{(n)} + \sum_i \left( n_i - \sum_k \lambda_k^{(n)} p_{ik} \right) p_{ij}. \tag{6}$$

Although spatially variant PSFs can be used for $p_{ij}$, spatially invariant PSFs have been used in the current work.

A close examination shows that (6) is the iteration term that minimizes the square errors of the SBP image constructed from the estimated source distribution. This can be seen if we recast the steepest descent iteration term from [15]:

$$\begin{aligned}\Delta\lambda_j^{(n)} &= -\varepsilon \nabla\chi^2\left(\lambda_j^{(n)}\right) \\ &= -\varepsilon \frac{\sum_i \partial\left(n_i - \sum_k \lambda_k^{(n)} p_{ik}\right)^2}{\partial \lambda_j^{(n)}} \\ &= 2\varepsilon \sum_i \left( n_i - \sum_k \lambda_k^{(n)} p_{ik} \right) p_{ij},\end{aligned} \tag{7}$$

where $\Delta\lambda_j^{(n)}$ is the displacement of the estimate in the iteration step, $\varepsilon$ is a positive coefficient used to control the iteration. When $\varepsilon = 0.5$, the second term on the right-hand side of (6) is obtained.

Since the PSF has a 3D distribution, 3D deconvolution must be performed in order to reconstruct 3D images. However, when the source distribution can be considered to be two-dimensional (2D), corresponding to the case of a sliced sample, 2D deconvolution is sufficient because there is no contamination from outside of the 2D plane. Thus, we have implemented both 2D and 3D deconvolution algorithms.

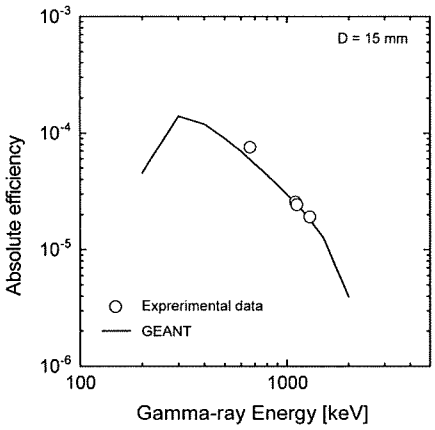


Fig. 3. Absolute efficiencies for obtaining the full-energy $\gamma$-ray peaks.

TABLE I
SPATIAL RESOLUTION OF THE RECONSTRUCTED IMAGE AND DERIVED TRANSITIONAL SPATIAL FREQUENCY OF THE FPSD OF THE SBP IMAGE

| Number of events | FWHM [mm] | | $f_c$ [mm$^{-1}$] | |
|---|---|---|---|---|
| | x-direction | z-direction | x-direction | z-direction |
| $1.0 \times 10^5$ | 4.9 | 11.4 | 0.16±0.02 | 0.06±0.01 |
| $5.0 \times 10^4$ | 6.0 | 12.9 | 0.15±0.02 | 0.05±0.01 |
| $1.0 \times 10^4$ | 10.3 | 14.2 | 0.12±0.03 | 0.04±0.01 |

## IV. PERFORMANCE OF THE PROTOTYPE

The absolute efficiencies for obtaining the full-energy $\gamma$-ray peaks from the sources 15 mm away from the center of the front detector are shown in Fig. 3, together with the values estimated by Monte Carlo simulation using a GEANT [16] code. The experimental values were derived from the experimental data mentioned in the next section. One can see that the GREI system has

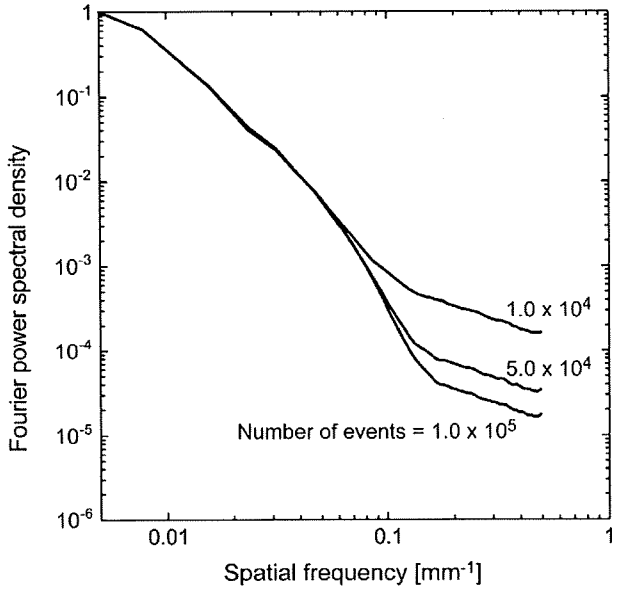


Fig. 4. Projection of the Fourier power spectral densities of the SBP images obtained by measuring $^{65}$Zn point-like source using the GREI system.

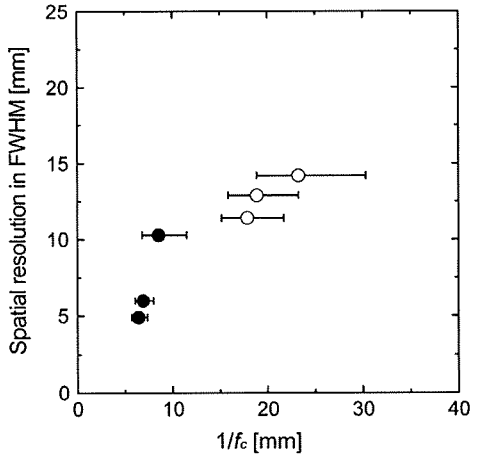


Fig. 5. Spatial resolution vs. $1/f_c$. Solid circle: x-direction, Open circle: z-direction.

significant efficiency between the energy range from ~200 keV to ~2 MeV.

The effect of the statistical noise on the spatial resolution achieved with the prototype system was investigated in terms of the Fourier power spectral density (FPSD) of the SBP image. A point-like source of $^{65}$Zn, which emits 1116 keV $\gamma$ rays, was placed 69 mm away from the center of the front detector, and then three SBP images were constructed in 3D space with the detected event numbers of $1.0 \times 10^4$, $5.0 \times 10^4$, and $1.0 \times 10^5$. Then the SBP images were analytically deconvolved with the PSF constructed using a GEANT code. The full widths at half maximum (FWHMs) of the reconstructed images of the point source are shown in Table I for each number of events. Fig. 4 shows the projection of the FPSDs onto the $x$-axis for the SBP images. One can see in the figure that there is a common component that decreases as the spatial frequency increases. This component is understood to represent the intrinsic characteristics of the GREI system. One can also see in Fig. 4 that there

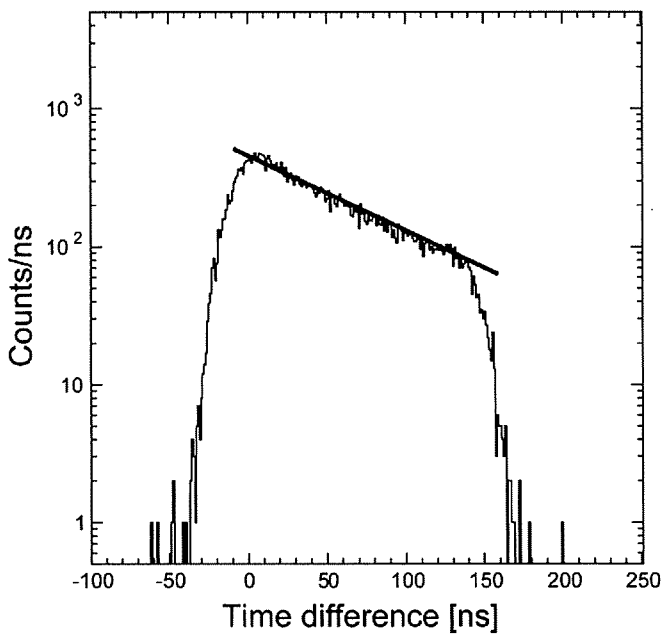


Fig. 6. Histogram of the time difference between the signals of the anode and cathode strips. The energy window was set at the 122-keV $\gamma$-ray peak of $^{152}$Eu. The solid line indicates a fit using an exponential function.

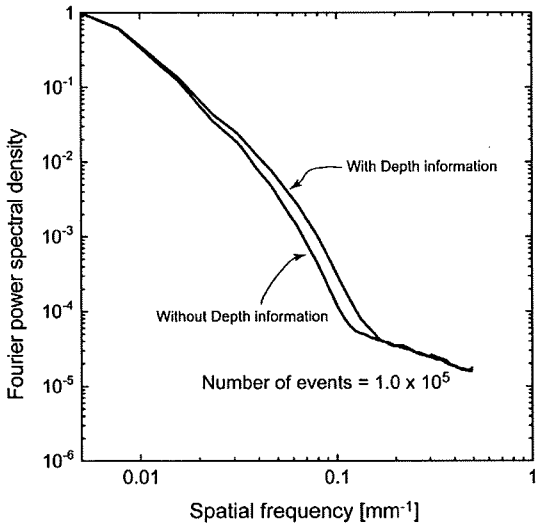


Fig. 7. Projection of the Fourier power spectral densities of the SBP images obtained by measuring $^{65}$Zn point-like source using the GREI system.

is another component significant in the high-frequency region, which is understood to be the statistical noise component because it decreases as the number of events increases. We defined the transitional spatial frequency $f_c$ (Table I), where the noise component is beginning to be dominant, by the positive peak of the second derivative of the FPSD curve. As a function of $1/f_c$, the spatial resolutions are plotted in Fig. 5. In the figure, one can see a positive correlation between the spatial resolution and $1/f_c$. However, the correlations for x- and z-direction seem to differ. If we can obtain the comprehensive relationship between the spatial resolution and $1/f_c$, the information would be useful to estimate the performance of the designed system without image reconstruction.

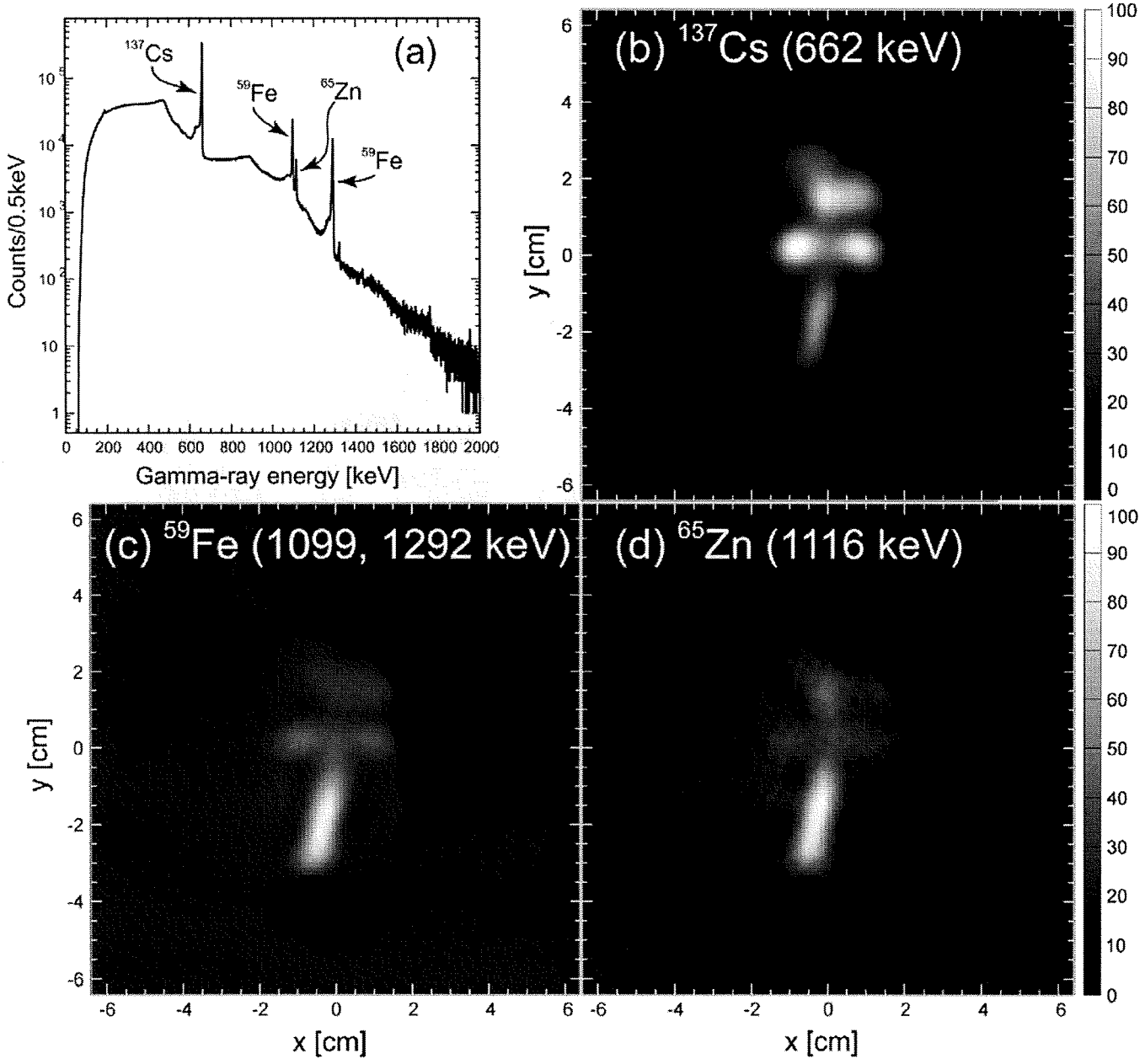


Fig. 8. Results of 2D imaging of the soybean sample.

In order to derive the depth position of the interaction from the time difference between the anode and cathode signals, the time difference was measured for each combination of the anode and cathode strips using a $\gamma$-ray source of $^{152}$Eu placed in front of the detector. Fig. 6 shows one of the histograms for the front detector with an energy window at the 122-keV $\gamma$-ray peak. The origin of the abscissa has been adjusted so that the time difference is 0 ns when the counts are maximum. The dependence of the counts on the time difference agreed well with the attenuation curve of 122-keV $\gamma$ rays in Ge crystals assuming that the time differences of 0 ns and 140 ns correspond to the depth positions of 0 mm and 10 mm, respectively. Considering this fact, we assigned a simple linear function of the time difference to derive the depth position; the position resolution is determined by the quality of the fit and the time resolution. Moreover, the spread of the timing spectrum was found to be identical even for the other $\gamma$-ray energies. Owing to this fact, the algorithm to derive the depth position has become very simple. This is an advantage of using CFDs, which generate the timing pulses independent of the amplitude of the input signals.

The effect of the depth measurement was examined in terms of the FPSD as mentioned above. Two SBP images were constructed with and without the depth information using the same data shown in Fig. 4 with $1.0 \times 10^5$ events. The FPSDs of the SBP images are shown in Fig. 7. One can see that the intrinsic characteristics of the system deteriorated without the depth information, though the statistical noise was of the same level. This result was consistent with the Monte Carlo simulation where the position resolution of depth measurement was 1 mm in FWHM.

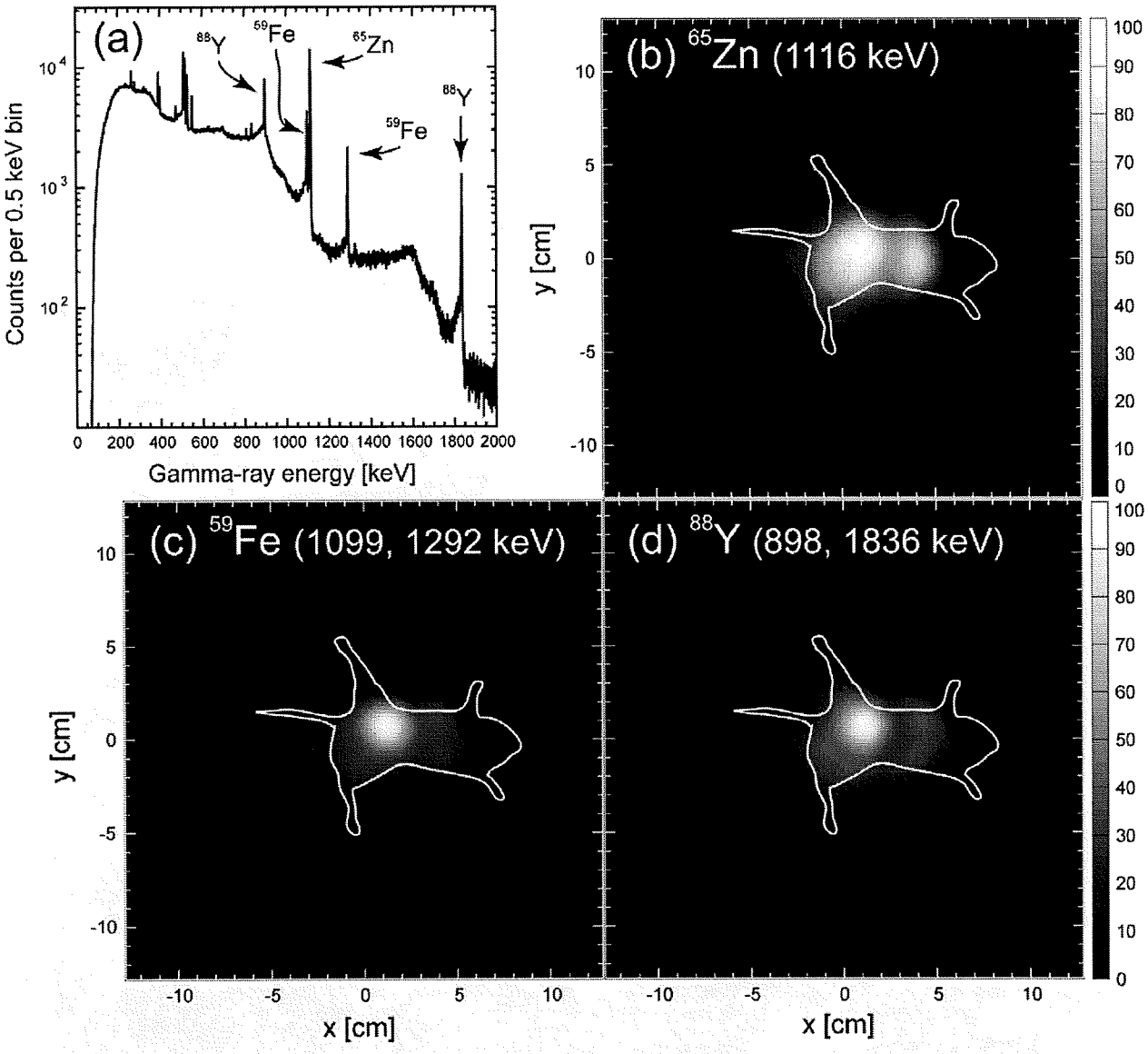


Fig. 9. Results of 2D imaging of the tumor-bearing mouse.

## V. Experiment With Biological Samples

We have performed experiments with two biological samples in order to demonstrate the capability of nondestructive imaging of a multitracer. The first sample was a soybean plant administered with 310-kBq $^{137}$Cs, 89-kBq $^{59}$Fe, and 20-kBq $^{65}$Zn. A photograph of the sample is shown in Fig. 10. The sample was fixed on a plane 15 mm away from the center of the front Ge detector. The measurement was carried out for 25 hours.

Fig. 8 shows the results of 2D imaging of the soybean sample. The energy windows were set at each peak position indicated in the $\gamma$-ray energy spectrum Fig. 8 to distinguish the radionuclides of $^{137}$Cs, $^{59}$Fe, and $^{65}$Zn. The 2D SBP images were constructed for each nuclide on the plane where the sample was fixed, assuming a 2D distribution, and then the analytical reconstruction method was used to deconvolve the 2D SBP images with the 2D PSFs. The resulting images successfully visualized the different behaviors of the nuclides. The $^{137}$Cs nuclide was distributed throughout the whole of the sample, because it is chemically analogous to K, while $^{59}$Fe and $^{65}$Zn remained near the root. The $^{65}$Zn nuclide was found at the tip of the stem to some extent, where the plant was actively growing, because Zn is required for cell division.

In addition, we note that there is a difference in the background structure of the images. This is due to the difference in the number of events obtained for each nuclide; $2.5 \times 10^6$, $3.4 \times 10^5$, and $7.3 \times 10^4$ for $^{137}$Cs, $^{59}$Fe, and $^{65}$Zn, respectively. The smaller the number of events, the larger the statistical noise component becomes, as mentioned in Section IV.

The second sample was a tumor-bearing mouse administered intravenously with a multitracer solution that includes 60-kBq $^{65}$Zn, 30-kBq $^{59}$Fe, and 10-kBq $^{88}$Y. The sample was fixed on a board and placed just under the front detector, which was installed with its front face down. The measurement was carried out for 95 hours.

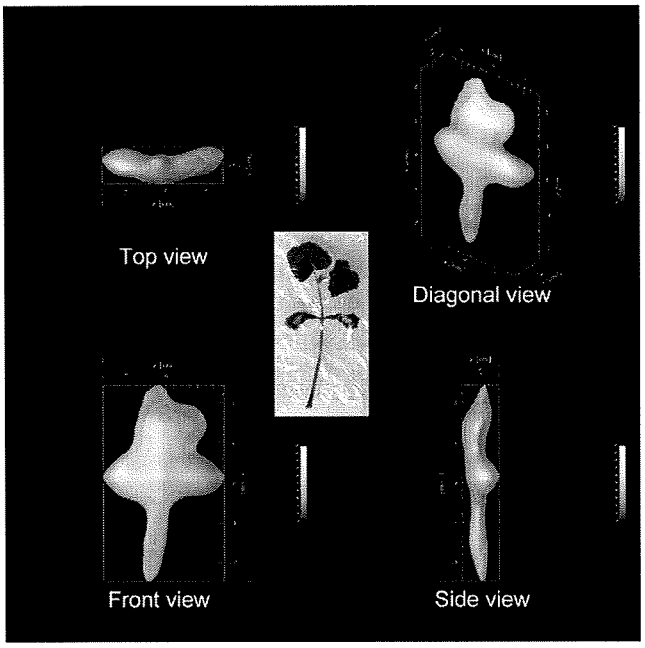


Fig. 10. Three-dimensional image of $^{137}$Cs distributed in the soybean sample. A photograph of the sample is also shown at the center.

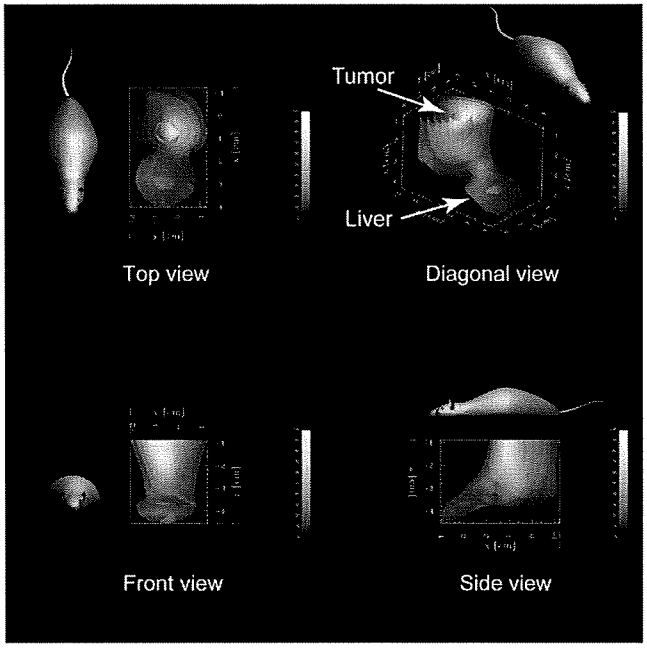


Fig. 11. Three-dimensional image of $^{65}$Zn distributed in the tumor-bearing mouse. The orientations of the sample are indicated by the mouse figures.

Fig. 9 shows the results of 2D imaging of the tumor-bearing mouse. As in the case of the soybean sample, the energy windows were set at each peak position indicated in the $\gamma$-ray energy spectrum Fig. 9 to distinguish the radionuclides of $^{65}$Zn,$^{59}$Fe, and $^{88}$Y. Then the 2D SBP images were constructed for each nuclide on the 2D plane that intersects the tumor part, and the SBP images were analytically deconvolved with the 2D PSFs. The resulting images are only "focused" images along the assumed plane, because the other parts of the sample have some contribution to the constructed 2D SBP images. Nevertheless, the accumulation of the nuclides in the tumor site was evident and $^{65}$Zn was also found in the liver. The results are consistent with those reported in [17]–[19].

We have performed 3D imaging of these samples, even though the samples were measured from a fixed direction. When the sample is sufficiently close to the front detector, the source distribution can be projected towards various directions because no mechanical collimator is used. This is a distinctive feature of a Compton camera. First, the 3D SBP images were constructed in 3D space, then the SBP images were deconvolved with the 3D PSFs.

Fig. 10 shows the result of 3D imaging of $^{137}$Cs in the soybean sample. The deconvolution was performed analytically. Since $^{137}$Cs was distributed throughout the whole sample, the shape of the sample can be recognized. However, there exists a warp in the reconstructed image, which may have been caused by the use of spatially invariant PSFs.

Fig. 11 shows the result of 3D imaging of $^{65}$Zn in the tumor-bearing mouse. In this case, we could not obtain any satisfactory images by analytical deconvolution. Thus, the reconstructed space was limited to only the region around the sample, and the iterative deconvolution was performed. The resulting image successfully visualized the accumulation of $^{65}$Zn in the tumor and the liver. However, the image has a similar warp to the 3D image of the soybean sample. Spatially variant PSFs should be incorporated to obtain more accurate images.

We were able to demonstrate the feasibility of using the GREI system for nondestructive imaging of multitracer. However, the measurement times taken to obtain the images would be unsuitable for practical imaging, although they can be shortened to about 10 hours if more intense $\gamma$-ray sources are used. Moreover, a higher spatial resolution would be desired to observe more fine structure. These demands would be met if the $\gamma$-ray tracking technique and pulse-shape analysis are implemented, which have been recently developed [20]. With these techniques implemented, the efficiency and the intrinsic characteristics are improved, thereby shortening the measurement time and improving the spatial resolution.

## VI. Summary

A prototype of a Compton camera, GREI, has been fabricated for nondestructive imaging of a multitracer. It is composed of two double-sided orthogonal-strip Ge detectors, and the efficiency is significant in the energy range from ~200 keV to 2 MeV. The timing method was used to derive the depth position of the $\gamma$-ray interaction with a resolution of ~1 mm FWHM. Both analytical and iterative image reconstruction methods were implemented for 2D and 3D imaging. A test experiment was performed to demonstrate the capability of the GREI system. The resulting images successfully visualized the different behavior of each nuclide for both the soybean and the mouse sample. Furthermore, 3D images were obtained even though the samples were measured from a fixed direction. However, there was some distortion in the 3D images, which may have been caused by the use of spatially invariant PSFs. Spatially variant PSFs should be incorporated to obtain more accurate 3D images. To make the GREI system suitable for practical imaging, $\gamma$-ray tracking technique and pulse-shape analysis should be implemented.

## REFERENCES


[1] S. Ambe, S. Y. Chen, Y. Ohkubo, Y. Kobayashi, M. Iwamoto, M. Yanokura, and F. Ambe, "Preparation of a radioactive multitracer solution from gold foil irradiated by 135 MeV/nucleon $^{14}$N ions," *Chem. Lett.*, pp. 149–152, 1991.

[2] S. Enomoto, "Development of multitracer technology and application studies on biotrace element research," *Biomed. Res. Trace Elem.*, vol. 16, pp. 233–240, 2005.

[3] V. Schönfelder, "A telescope for soft gamma ray astronomy," *Nucl. Instrum. Methods*, vol. 107, pp. 385–394, 1973.

[4] R. W. Todd, J. M. Nightingale, and D. B. Everett, "A proposed $\gamma$ camera," *Nature*, vol. 251, pp. 132–134, 1974.

[5] G. W. Phillips, "Gamma-ray imaging with Compton cameras," *Nucl. Instrum. Methods Phys. Res. B*, vol. B99, pp. 674–677, 1995.

[6] Y. F. Yang, Y. Gono, S. Motomura, S. Enomoto, and Y. Yano, "A Compton camera for multitracer imaging," *IEEE Trans. Nucl. Sci.*, vol. 48, no. 3, pp. 656–661, Jun. 2001.

[7] Y. F. Yang, Y. Gono, S. Motomura, S. Enomoto, and Y. Yano, "Monte Carlo simulations of the performance of a Compton camera consisting of position sensitive germanium detectors," *Nucl. Instrum. Methods Phys. Res. A*, vol. A482, pp. 806–813, 2002.

[8] M. Momayezi, W. K. Warburton, and R. Kroeger, "Position resolution in a Ge-strip detector," *Proc. SPIE*, vol. 3768, pp. 530–537, 1999.

[9] M. Amman and P. N. Luke, "Three-dimensional position sensing and field shaping in orthogonal-strip germanium gamma-ray detectors," *Nucl. Instrum. Methods Phys. Res. A*, vol. A452, pp. 155–166, 2000.

[10] E. A. Wulf, J. Ampe, W. N. Johnson, R. A. Kroeger, J. D. Kurfess, and B. F. Phlips, "Depth measurement in a germanium strip detector," *IEEE Trans. Nucl. Sci.*, vol. 49, no. 4, pp. 1876–1880, Aug. 2002.

[11] E. A. Wulf, B. F. Phlips, W. N. Johnson, R. A. Kroeger, J. D. Kurfess, and E. I. Novikova, "Germanium strip detector Compton telescope using three-dimensional readout," *IEEE Trans. Nucl. Sci.*, vol. 50, no. 4, pp. 1182–1189, Aug. 2003.

[12] S. Motomura, S. Enomoto, Y. Gono, and Y. Yano, "Effect of electrode design on depth-of-interaction sensitivity in two-dimensionally segmented planar germanium detectors," to be submitted.

[13] R. C. Rohe, M. M. Sharfi, K. A. Kecevar, J. D. Valentine, and C. Bonnerave, "The spatially-variant backprojection point kernel function of an energy-subtraction Compton scatter camera for medical imaging," *IEEE Trans. Nucl. Sci.*, vol. 44, no. 6, pp. 2477–2482, Dec. 1997.

[14] P. Gilbert, "Iterative methods for the three-dimensional resonstruction of an object from projections," *J. Theor. Biol.*, vol. 36, pp. 105–117, 1972.

[15] W. H. Press, S. A. Teukolsky, W. T. Vetterling, and B. P. Flannery, *Numerical Recipes in C: The Art of Scientific Computing*, 2nd ed. Cambridge, U.K.: Cambridge Univ. Press, 1992, p. 681.

[16] Detector Description and Simulation Tool, GEANT, CERN, Geneva, 1993.

[17] H. Tamano, S. Enomoto, B. Liu, and A. Takeda, "Tumor accumulation of radioactive trace elements: A multitracer study," *Biomed. Res. Trace Elem.*, vol. 12, pp. 96–101, 2001.

[18] H. Tamano, S. Enomoto, N. Oku, and A. Takeda, "Preferential uptake of zinc, manganese and rubidium in rat brain tumor," *Nucl. Med. Biol.*, vol. 29, pp. 505–508, 2002.

[19] A. Takeda, H. Tamano, S. Enomoto, and N. Oku, "Zinc-65 imaging of rat brain tumors," *Cancer Res.*, vol. 61, pp. 5065–5069, 2001.

[20] K. Vetter, M. Burks, and L. Mihailescu, "Gamma-ray imaging with position-sensitive HPGe detectors," *Nucl. Instrum. Methods Phys. Res. A*, vol. A525, pp. 322–327, 2004.

Available online at www.sciencedirect.com
ScienceDirect
Geochimica et Cosmochimica Acta 71 (2007) 3458–3475
Geochimica et Cosmochimica Acta
www.elsevier.com/locate/gca

# Comparison of reductive accumulation of Re and Os in seawater–sediment systems

Yoshiro Yamashita [a], Yoshio Takahashi [a,*], Hiromitsu Haba [b], Shuichi Enomoto [b], Hiroshi Shimizu [a]

[a] *Department of Earth and Planetary Systems Science, Graduate School of Science, Hiroshima University, Higashi-Hiroshima, Hiroshima 739-8526, Japan*
[b] *RIKEN (The Institute of Physical and Chemical Research), Wako, Saitama 351-01, Japan*

Received 3 April 2006; accepted in revised form 3 May 2007; available online 10 May 2007

**Abstract**

In order to understand the fractionation of Re and Os in marine environments, their removal from artificial seawater to Tokyo Bay sediments is studied using a multitracer technique. The chemical processes of the removal of Re and Os are also estimated based on their speciation analyses by X-ray absorption fine structure (XAFS) spectroscopy. The partitioning experiments, which use the multitracer technique, provide information on Re and Os regarding (i) their distributions between artificial seawater–sediment systems, (ii) their complexation with humic acid, and (iii) their carriers in sediments. In addition, XAFS spectroscopy provides direct information on the chemical states of Re and Os in the sediments.

In an artificial seawater–sediment system containing a multitracer, Re is removed from the artificial seawater only under a reducing environment. The speciation of Re by X-ray absorption near-edge structure (XANES) suggests that the majority of Re remains as $ReO_4^-$ in the artificial seawater even under highly reducing conditions, during laboratory time scale (about 2 weeks). Moreover, XANES simulation shows that some Re exists at a lower oxidation state, such as $ReO_2$, in the reducing sediment. These results can be explained by the slow kinetics of the reaction which is similar to those suggested by previous geochemical studies.

In contrast, Os is readily removed from the artificial seawater into sediments under various redox conditions. Even under oxic conditions, a large fraction of Os is removed from the artificial seawater to sediments without organic matter. Based on the Os XANES study, it is confirmed that the oxidation states of Os incorporated in the reducing sediment and oxic sediment are trivalent and tetravalent, respectively. Sequential extraction suggests that the main carrier of Os in the organic-rich sediment is either ferromanganese oxides or organic matter, and that the Os in these two fractions may correspond to hydrolyzed insoluble Os species and Os species interacting with organic matter, at lower valence, respectively. The results of distribution study of Os in the absence and presence of humic acid (HA) also imply that Os assumes more than one chemical species, and a small fraction of Os may interact with HA in the experimental system. Meanwhile, extended X-ray absorption fine structure (EXAFS) confirms that the first neighboring atom of Os in the reducing sediment is oxygen. If Os(VIII) is the main dissolved species in seawater, as is expected thermodynamically, reductive removal may control the enrichment of Os in the sediment. Osmium, which is removed as Os(IV), is reduced further to Os(III) by a diagenetic process and may be complexed with organic matter in the reducing sediment.

The results of the removal behaviors of Re and Os obtained in the current study show that Re can be removed from the artificial seawater only under highly reducing conditions within 2 weeks, but Os removal from the artificial seawater can be found under various redox conditions. Thus, a high $^{187}Re/^{188}Os$ ratio can occur only in reducing sediments, such as black shales. The high $^{187}Re/^{188}Os$ ratio, in turn, makes black shales suitable for Re–Os dating. In contrast, authigenic sediments (and minerals) under oxic environments can enrich Os, but since Re is not distributed to the sediments under oxic conditions,

* Corresponding author. Fax: +81 82 424 0735.
*E-mail address:* ytakaha@hiroshima-u.ac.jp (Y. Takahashi).


doi:10.1016/j.gca.2007.05.003